npj | Quantum Materials

www.nature.com/npjquantmats

ARTICLE OPEN

Emergent long-range magnetic order in ultrathin (111)-oriented $LaNiO_3$ films

Margaret M. Kane[1,2✉], Arturas Vailionis[3,4], Lauren J. Riddiford[2,5], Apurva Mehta[6], Alpha T. N'Diaye[7], Christoph Klewe[7], Padraic Shafer[7], Elke Arenholz[7] and Yuri Suzuki[2,5✉]

The emergence of ferromagnetism in materials where the bulk phase does not show any magnetic order demonstrates that atomically precise films can stabilize distinct ground states and expands the phase space for the discovery of materials. Here, the emergence of long-range magnetic order is reported in ultrathin (111) $LaNiO_3$ (LNO) films, where bulk LNO is paramagnetic, and the origins of this phase are explained. Transport and structural studies of LNO(111) films indicate that NiO_6 octahedral distortions stabilize a magnetic insulating phase at the film/substrate interface and result in a thickness-dependent metal–insulator transition at $t = 8$ unit cells. Away from this interface, distortions relax and bulk-like conduction is regained. Synchrotron x-ray diffraction and dynamical x-ray diffraction simulations confirm a corresponding out-of-plane unit-cell expansion at the interface of all films. X-ray absorption spectroscopy reveals that distortion stabilizes an increased concentration of Ni^{2+} ions. Evidence of long-range magnetic order is found in anomalous Hall effect and magnetoresistance measurements, likely due to ferromagnetic superexchange interactions among Ni^{2+}–Ni^{3+} ions. Together, these results indicate that long-range magnetic ordering and metallicity in LNO(111) films emerges from a balance among the spin, charge, lattice, and orbital degrees of freedom.

npj Quantum Materials (2021)6:44 ; https://doi.org/10.1038/s41535-021-00345-2

INTRODUCTION

Complex oxide materials exhibit a wide range of correlated electron behavior representing the delicate balance of charge, spin, orbital, and lattice degrees of freedom. External parameters such as electric field, magnetic field, or strain can tune the material to exhibit correlated phenomena, including ferromagnetism[1–4] and superconductivity[5,6]. In a few complex oxide materials, the ferromagnetic order has been stabilized in thin film form, although the bulk phase has no long-range magnetic order. $LaCoO_3$ thin films exhibit ferromagnetism ($T_c = 70$ K)[1,7–9], while bulk phases are diamagnetic at low temperatures and paramagnetic at higher temperatures. Similar stabilization of a ferromagnetic ground state is found in $PrCoO_3$[2,10]. Despite various experimental studies, the origin of this emergent ferromagnetism is still not well understood.

$LaNiO_3$ (LNO), a paramagnetic metal at all temperatures in the bulk, has elicited attention because theory predicts interesting topological phases in (111)-oriented LNO grown on $LaAlO_3$ (LAO)[11–14]. Unlike LNO, other rare-earth nickelates of the form $RENiO_3$ (RE = rare earth) have temperature-dependent metal–insulator and magnetic transitions. While a suppression of metallicity has been achieved in (001)-oriented LNO films with thicknesses of $t = 2 - 4$ unit cells (u.c.)[15–22], no magnetic order has ever been observed. Recently, there has been a report of ferromagnetism in a 10-u.c.-thick (111)-oriented LNO film[23], but the underlying mechanisms of this ferromagnetism were not clear. Understanding the origin of the emergent long-range magnetic order in LNO(111) films would enable us to design and tune such correlated behavior and explore interactions in possible topological phases.

Here, we report the emergence of long-range magnetic order in LNO films grown on LAO(111) in a wide range of thicknesses ($t = 8 - 26$ u.c.), in both insulating and metallic samples. The anomalous Hall effect and hysteretic magnetoresistance (MR) indicate long-range magnetic order only present in the (111) direction. The (111) interface limits the strain relaxation required by the lattice mismatch between substrate and film, causing a distortion of the NiO_6 octahedra. An expansion near the substrate–film interface is observed via x-ray diffraction measurements and dynamical x-ray diffraction simulations. X-ray absorption spectroscopy reveals an increased concentration of Ni^{2+} ions in ultrathin films, replacing Ni^{3+} ions observed in thicker films and bulk LNO. Together, the structural changes at the LNO/LAO(111) interface and the increased concentration of Ni^{2+} ions in ultrathin LNO films likely facilitate ferromagnetic superexchange interactions among Ni^{2+} and Ni^{3+} ions. The emergent magnetic order in ultrathin LNO(111) films, therefore, relies both on the growth constraints imposed by lattice mismatch in the (111) interface geometry and on the presence of Ni^{2+} ions.

RESULTS

Structural characterization

In order to determine the underlying mechanism responsible for the emergent magnetic ordering, we performed careful structural, chemical, and transport characterization. Structural characterization via laboratory and synchrotron x-ray diffraction measurements confirm the excellent crystalline quality and fully coherent growth of all films. Figure 1a shows symmetrical x-ray diffraction scans around LNO/LAO(222) Bragg peaks. The LNO(222) peak, on the left of the LAO(222) substrate peak, signifies the expected

[1]Department of Materials Science and Engineering, Stanford University, Stanford, CA, USA. [2]Geballe Laboratory for Advanced Materials, Stanford University, Stanford, CA, USA. [3]Stanford Nano Shared Facilities, Stanford University, Stanford, CA, USA. [4]Department of Physics, Kaunas University of Technology, Kaunas, Lithuania. [5]Department of Applied Physics, Stanford University, Stanford, CA, USA. [6]SLAC National Accelerator Laboratory, Menlo Park, CA, USA. [7]Advanced Light Source, Lawrence Berkeley National Laboratory, Berkeley, CA, USA. ✉email: mmkane@stanford.edu; ysuzuki1@stanford.edu

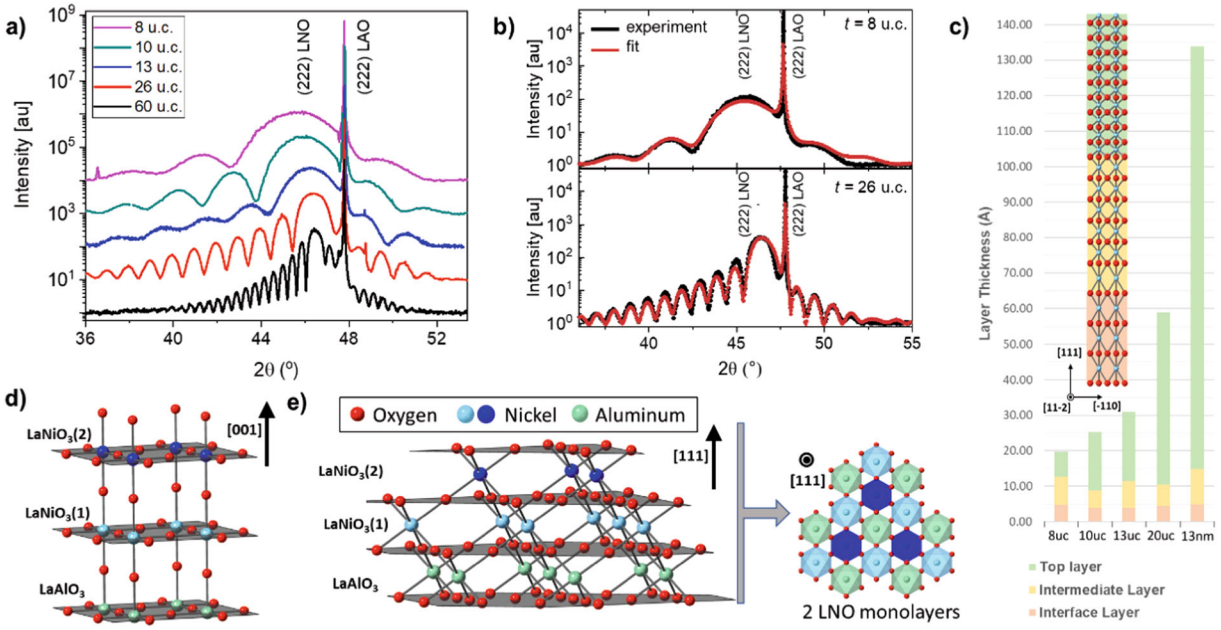

Fig. 1 Structural characterization of (111)-oriented $LaNiO_3$. a Experimental x-ray diffraction profiles of ultrathin $LaNiO_3$ (LNO) films around the (222) peak. **b** Representative x-ray diffraction fits of LNO films. The 8 and 26 u.c. films are modeled as three layers, with the largest distortion of the unit cell in the interfacial layer. **c** Results of the dynamical x-ray diffraction simulations, highlighting the distortions of the NiO_6 octahedra, the thickness of the distorted layers, and the overall thickness of the films. Numerical values are listed in Supplemental Table 2. Schematic diagram of oxygen octahedra connectivity and LNO layer buildup along **d** [0 0 1] and **e** [1 1 1] direction. Right: two monolayers of $LaNiO_3$. The light blue indicates Ni atoms in the first monolayer, and dark blue indicates Ni atoms in the second monolayer. Note La atoms are not pictured here. Strong coupling of oxygen bonds across the LNO/LAO(111) interface imposes restrictions on NiO_6 octahedra in the first few LNO monolayers that are controlled by the underlying symmetry of the LAO lattice.

overall compressive in-plane strain. The thickness fringes extending around the LNO(222) Bragg peak indicate high crystalline quality of the films and the uneven fringe intensity distribution imply that there is a variable out-of-plane interatomic spacing along the film thickness[24].

To quantify the variation of the LNO interplanar spacing along the [1 1 1] direction, we have employed dynamical x-ray diffraction modeling of the X-ray powder diffraction profiles of LNO/LAO(111) thin films. X-ray diffraction calculations were carried out using the GID sl_program for simulating dynamical x-ray diffraction from strained crystals, multilayers, and superlattices, developed by Stepanov[25]. LNO(111) films can be fit by dynamical x-ray diffraction as three layers (see Fig. 1b): an interfacial layer with the largest out-of-plane *d*-spacing, followed by an intermediate layer with less expanded d_{111} spacing, and finally a bulk-like region where deformations of the NiO_6 octahedra are diminished and the mismatch strain is accommodated by octahedral rotations. In order to accommodate coherent epitaxial strain, NiO_6 octahedra are rotated differently than in bulk LNO in all three layers. Although the lattice parameter should change continuously and not form distinct layers, we were able to successfully fit the x-ray diffraction profiles using a three-layer model.

Our x-ray diffraction profiles show a dramatic change in the out-of-plane lattice parameter of the LNO films with depth. Bulk LNO has pseudocubic unit cell of $a_{LNO} = 3.86$ Å and bulk LAO has a psuedocubic lattice parameter of $a_{LAO} = 3.79$ Å giving an expected lattice mismatch of ~−1.8%. In this paper, we define one unit cell in a (111)-oriented film as the distance between two (111) planes, or as $d_{111} = a_{001}/\sqrt{3} = 2.23$ Å. Analysis of the (111)-oriented films show an interfacial layer with an average calculated thickness of 2 u.c. and a remarkable 16% expansion of the d_{111} interplanar distance as compared to the bulk-like thin film region. The next, intermediate layer has an average calculated thickness of 3 u.c. and a 3% d_{111} expansion. The topmost, most bulk-like layer has a pseudocubic out-of-plane lattice constant of about $a_{LNO} = 3.821$ Å consistent across samples of all thicknesses. Representative x-ray diffraction simulations of the 8 and 26 u.c. samples are shown in Fig. 1b. Simulations that assume a lattice parameter change in the surface layer or a film of uniform lattice parameter did not fit as well to the experimental data. Fit parameters and plots for all samples are presented in Supplemental Table 1 and Supplemental Figure 1.

The large lattice distortion observed at the LNO/LAO interface is likely due to the nature of the interfacial bonding. Because the NiO_6 octahedra are connected across the interface via three oxygen bonds, they are more constrained than those in (001)-oriented films (see Fig. 1d, e). The enhanced interfacial bonding at the (111) interface inhibits octahedral rotations that normally relieve the interfacial mismatch strain and instead favors a physical deformation of the octahedra, considerably expanding it along the [1 1 1] direction. In addition, there is much less octahedra connectivity within the single (111) plane (Fig. 1e); they are instead more directly affected by octahedra in the layer above and below them. By contrast, a synchrotron x-ray diffraction study of (001)-oriented LNO films by Fowlie et al. shows no enlargement of the out-of-plane lattice parameter for films 5 u.c. to 10 nm thick[19], indicating effective strain accommodation by octahedral rotations. A dramatic change in film properties due to distortion of the unit cell fits well with the past work[15–21,26,27]. The structural model that we derive from dynamical x-ray diffraction simulations suggests that the LNO unit-cell symmetry is lowered at the interface due to octahedral deformations. It is known that the symmetry lowering at an interface can result in various emergent functionalities: piezoelectric[28,29], pyroelectric[30], and ferroelectric effects[31,32]. In fact, Doennig et al. predict the emergence of magnetic ordering in reduced symmetry LNO[11].

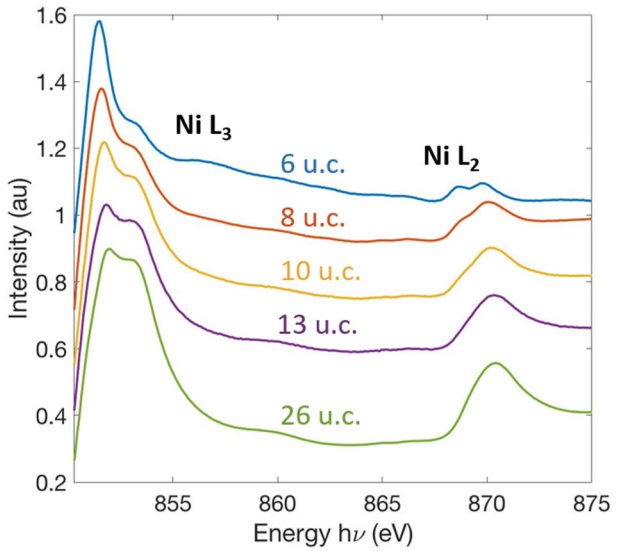

Fig. 2 X-ray absorption spectroscopy results of (111)-oriented $LaNiO_3$ films taken at ALS beamline 6.3.1. Note that the La peak located at 849 eV has been subtracted out using peak fitting software. Splitting of the Ni L_2 peak indicates an increased concentration of Ni^{2+} ions in the $LaNiO_3$ films.

Chemical valence characterization

Chemical valence characterization, performed using x-ray absorption spectroscopy (XAS), indicates that the valence of ultrathin (111) LNO films differs from bulk LNO. We see an increase in Ni^{2+} cations as films get thinner (see Fig. 2), as shown by an increase in the Ni L_3 edge peak at ~852 eV and a splitting of the Ni L_2 edge peak near 870 eV. The increasing intensity of the Ni^{2+} peak (852 eV) compared to the Ni^{3+} peak (854 eV) qualitatively shows that there is a higher concentration of Ni^{2+} near the substrate–film interface. Previous work by Anada et al. does not reveal any evidence of Ni^{2+} ions in LNO films grown on (001)-oriented LAO, although they observe a high concentration of Ni^{2+} ions in corresponding LNO films grown on (001)-oriented $SrTiO_3$[33]. The increased concentration of Ni^{2+} ions is likely due to either oxygen vacancies or oxygen ligand holes, which have been linked to insulating behavior in LNO films[34]. Although these two potential sources of Ni^{2+} ions are distinct, they are difficult to differentiate. Here, we do not have sufficient evidence to suggest which one dominates in ultrathin LNO films. In any case, XAS data show that the LNO/LAO(111) interface is populated with an increased concentration of Ni^{2+} ions.

Electronic transport characterization

We also observe a change in the electronic properties in the thinnest samples: resistivity measurements of LNO(111) films reveal a thickness-dependent metal–insulator transition when the film thickness decreases <8 u.c. ($t = 17.8$ Å), see Fig. 3. The 6- and 8-u.c.-thick film resistivity can be modeled with thermally activated behavior at higher temperatures and 3D variable-range hopping at lower temperatures (see Fig. 3b, c). This indicates that the distorted LNO at the interface is insulating.

For the 6- and 8-u.c.-thick samples, the thermally activated behavior is described by an Arrhenius relation for carriers:

$$\sigma = \sigma_0 \exp(-\Delta E/kT) \quad (1)$$

where σ_0 is Drude conductivity, and ΔE is the thermal activation energy. See Supplemental Table 2 for the values obtained from the fit.

At lower temperatures, the 8 u.c. sample fits well to a variable-range hopping model where conduction occurs through inelastic hopping to states closer in energy[35]:

$$\sigma = \sigma_0 \exp\left(-T_0/T\right)^{1/(d+1)} \quad (2)$$

where T_0 is related to the density of states at the Fermi level and the spread of the wavefunction of the localized state, and d is the dimensionality of the system. Our sample fits best when $d = 3$, indicating that the transport behavior is not due to strong localization from a dimensional shift ($d = 2$) as has been observed in other (001)-oriented LNO films[17,20,22,33]. Because of instrument limitations, the 6 u.c. sample became too resistive to measure at 125 K. We propose that this insulating LNO is present in all our samples, but as the film thickens, the undistorted, bulk-like LNO dominates the transport. Additional details about these fits can be found in Supplemental Table 2.

In the 10, 13, and 26 u.c. samples, we observe an upturn in the resistivity at ~150, 70, and 25 K, respectively. Previous work on (001)-oriented LNO samples show a similar upturn in resistivity[17,18]. Moon et al. were able to fit the resistivity data from (001)-oriented LNO grown on various substrates to a model of weak localization described by a localization interaction model for a disordered metal in the 3D limit[17], but our resistivity data lack the characteristic curvature and does not fit well to this model.

In addition to interfacial Ni^{2+} and structural distortions noted above, we observe magnetic ordering through the anomalous Hall effect and hysteretic MR in samples 8–26 u.c. thick (Fig. 4). The Hall effect signal can be described using the equation:

$$\rho_{xy} = R_0 B + 4\pi R_S M \quad (3)$$

where the first term representing the ordinary Hall effect is proportional to the external magnetic field (with R_0 as the ordinary Hall coefficient) and the second term representing the anomalous Hall effect is proportional to the film magnetization (with R_S as the anomalous Hall coefficient (AHC)). The AHC represents both intrinsic contributions from the Berry phase curvature and extrinsic skew-scattering or side-jump mechanisms[36]. We observe nonlinearity in Hall effect measurements, with hysteretic behavior in 8–26 u.c. <~30 K, suggesting the emergence of spontaneous magnetization. The consistent onset temperatures support the idea of a magnetic phase of the same origin in all films. Figure 4a shows the behavior of the 10 u.c. film from $T = 2$ to 50 K. After subtracting the linear ordinary Hall effect contribution, we are left with clear loops (see Fig. 4b). The increase in coercivity and saturation resistance with decreasing temperature follows the expected behavior for a ferromagnet. Because the measured signal decreases with increasing film thickness (see Fig. 4c), it is likely that this magnetic phase is isolated to the distorted, insulating layer present in all films at the interface. As films get thicker, more current passes through the conducting bulk-like portion of the film, thus diminishing the transport contribution from the interface.

In addition, we observe a change in the sign of the AHC (R_S) in the 26-u.c.-thick LNO(111) film compared to thinner films. Studies of other systems that observe a thickness-dependent change in the AHC attribute the change in sign to either extrinsic skew-scattering and side-jump mechanisms[37–39] or to intrinsic changes in the band structure and the k-space Berry curvature of the material[40,41]. Simulations predict topological features in LNO grown on (111)-oriented LAO[11–14], so it is possible that the negative AHC results from an evolution of band structure with thickness in ultrathin LNO films. However, we are unable to determine the cause of this change in the AHC and leave that to future work.

Longitudinal MR measurements, taken with the field out of plane, show hysteresis at $T = 30$ K and a crossover from positive to negative MR as temperature decreases. A representative set of curves for a $t = 10$ u.c. sample is shown in Fig. 4d. At high temperatures, the MR has the expected parabolic form of ordinary

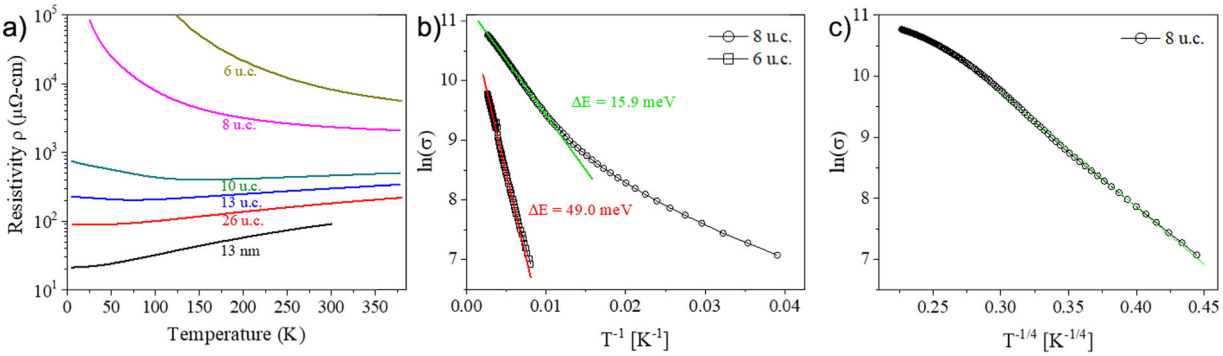

Fig. 3 Temperature-dependent electronic transport data for (111)-oriented $LaNiO_3$. a Resistivity versus temperature for 6 u.c. to 13-nm-thick films. **b** Arrhenius thermal activation of carriers fit the high-temperature data for insulating samples. **c** 3D variable-range hopping fit to low-temperature data for insulating samples. The samples became too insulating to measure at 125 K for the 6 u.c. sample and at 25 K for the 8 u.c. sample.

MR. As the temperature decreases, we observe an increasingly negative contribution to the longitudinal MR, which we attribute to the emergence of ferromagnetism. Negative MR is reported for (001)-oriented LNO films on $SrTiO_3$[20] and $(LaAlO_3)_{0.3}$ $(Sr_2AlTaO_6)_{0.7}$ (LSAT)[15] and is attributed to the suppression of weak localization by a magnetic field, but our resistivity data suggest that weak localization, associated with a simple, negative parabolic MR, alone does not explain the data.

Interestingly, below ~20–25 K the 10–26 u.c. samples show a suppression in resistivity after the external field switches sign (Fig. 4d). We would expect scattering from magnetic domain walls to be a source of spin-dependent scattering, thereby increasing resistivity. Notably, LNO(111) grown on LAO has been observed to be an improper ferroelectric[31]. Ferroelectric domain walls have exhibited increased conductivity[42–44] that is attributed to carrier accumulation at domain walls to screen polarization discontinuities and to the local modification of band structure[44]. This suppression of MR after the applied field changes sign is consistent with the results published by Asaba et al.[23] and with domain wall switching observed in antiferromagnetic $Nd_2Ir_2O_7$ thin films[45]. Similar behavior has been attributed to edge-state transport via chiral conducting modes in the topological insulator $SmBi_6$[46] and $Bi_2Te_{3-y}Se_y$[47]. However, further evidence of the emergence of Dirac electrons is needed to justify such conclusions in ultrathin LNO(111) films.

DISCUSSION

We can describe the electronic and magnetic behavior of the 8–26 u.c. LNO samples in terms of a strained, magnetic, insulating layer close to the film/substrate interface and a paramagnetic conducting layer on top. The first few unit cells of highly distorted LNO(111) have a modified symmetry and altered bond lengths and angles (e.g., Ni–O–Ni). These structural changes at the interface result in modifications of the exchange interactions among Ni^{2+}–Ni^{3+} ions, leading to a spontaneous magnetic moment. The Goodenough–Kanamori rules dictate that a low-spin $Ni^{2+}(3d^8)$–$Ni^{3+}(3d^7)$ exchange can give ferromagnetic ordering for 180° superexchange[48]. Together, the negative MR and the large hysteresis in the anomalous Hall effect suggest long-range magnetic order in LNO(111) films, and could indicate either ferromagnetic or antiferromagnetic ordering. We were unable to detect a ferromagnetic signal in the films above the noise level of a superconducting quantum interference device magnetometer and x-ray magnetic circular dichroism (XMCD) measurement at ALS. The limitations due to background noise of these measurement techniques mean that the absence of magnetic signal does not preclude ferromagnetism in the samples. Because of this, Hall measurements are an ideal probe for our LNO(111) samples because the magnitude of the signal is inversely proportional to the thickness.

In summary, we have observed the emergence of long-range magnetic ordering at the film–substrate interface in ultrathin (111)-oriented LNO thin films up to 26 u.c. Synchrotron x-ray diffraction and dynamical x-ray diffraction simulations indicate substantial elongation of the unit cell in the [1 1 1] direction near the interface. An increased presence of Ni^{2+} ions at the interface, insulating behavior in films $t \leq 8$ u.c., the anomalous Hall effect, and negative hysteretic MR indicate the presence of a distinct phase in LNO(111) in this region at the interface that hosts both insulating and magnetic behavior. This magnetic phase has a magnetic transition temperature of 30 K and likely comes from superexchange interactions among Ni^{2+} and Ni^{3+} ions. Such emergent magnetism provides a model system for the understanding of magnetic ordering in low dimensions and future spin-based architecture. These results also suggest that the particular distortions present in (111)-oriented films allow us to access emergent functionalities in materials that are unavailable in bulk or (001)-oriented thin films.

METHODS

Growth

LNO thin films were grown with thicknesses from 6 to 26 u.c. thick on $5 \times 5 \times 0.5$ mm^3 $LaAlO_3$ (111) single crystal substrates. In this paper, we define 1 u.c. as the distance between (111) planes, or $d_{111} = a_{LNO}/\sqrt{3} = 2.23$ Å, where a_{LNO} is the pseudocubic lattice parameter of LNO. Films were deposited using pulsed laser deposition with a 248-nm KrF laser operating at a fluence of 0.8 mJ/cm^2 and in an oxygen partial pressure of 20 mTorr on substrates heated to 780 °C. To achieve smooth (111)-oriented films, we used an interval pulsed laser deposition technique, where one deposits ~1 u.c. worth of material quickly (10 Hz) and then waits for the in situ reflective high-energy electron diffraction signal intensity to recover and stabilize. Thin film surface morphology was characterized by an atomic force microscope and exhibited low root mean square roughness (0.064–0.285 nm). A typical scan is shown as Supplemental Figure 2.

Characterization

Experimental x-ray diffraction data from ultrathin LNO(111) films were collected at beamline 7-2 at the Stanford Synchrotron Radiation Lightsource, SLAC National Accelerator Laboratory. X-ray diffraction profiles were matched with the profiles calculated using dynamical x-ray diffraction simulations, allowing us to precisely evaluate variations of the out-of-plane lattice parameter throughout the entire film thickness.

X-ray absorption spectroscopy measurements in total electron yield (TEY) mode were carried out at beamlines 4.0.2 and 6.3.1 at the Advanced Light Source, Lawrence Berkeley National Lab. Data were collected with a flying scan, where measurements were taken as the photon energy was continuously varied. Spectra were recorded with

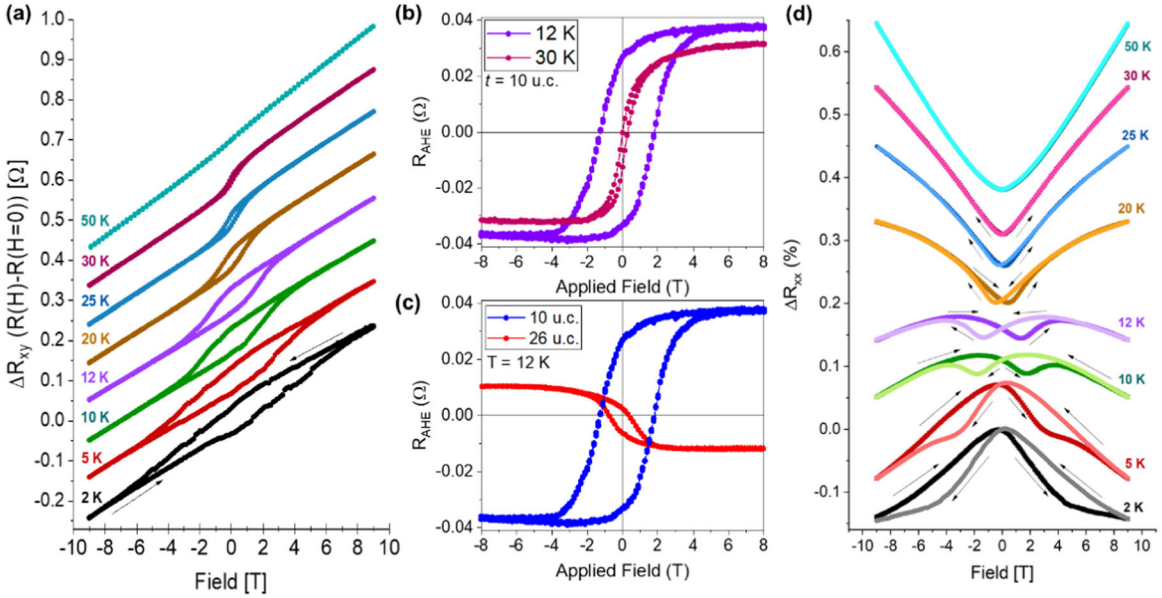

Fig. 4 Field-dependent electronic transport measurements of (111)-oriented $LaNiO_3$. a Hall effect results at various temperatures for 10-u.c.-thick LNO(111). Scans are shifted for visibility and arrows indicate the direction of scan, field cooled at $H = 9$ T, **b** anomalous Hall effect loops at various $T = 12, 30$ K, linear ordinary Hall effect has been subtracted, **c** anomalous Hall effect loops for $t = 10, 26$ u.c., linear ordinary Hall effect has been subtracted, **d** magnetoresistance at various temperatures of 10 u.c., (111)-oriented $LaNiO_3$, field cooled at $H = 9$ T. Magnetoresistance ($\Delta R_{xx} = (R(H) - R_0)/R_0$) results are shifted for visibility and arrows indicate the direction of scan.

both positive and negative photon helicity, and XMCD spectra were calculated from their difference. These measurements enabled us to probe cation valence in samples within the TEY probe depth of ~5 nm. Because of the proximity of the La $M_{4,5}$ edge to the Ni L_3 peak, we fitted and subtracted the La peak from the collected data. Comparison of the peak location, shape, and relative intensity among peaks with the reference data allowed us to probe how the concentration of Ni^{2+} and Ni^{3+} ions differs between samples.

Transport measurements were performed on a Quantum Design Physical Property Measurement system using van der Pauw and Hall bar configurations. Resistivity versus temperature data were collected while cooling. Hall measurements and longitudinal MR measurements were performed on samples patterned into a Hall bar structure using photolithography and Ar ion milling. AuPd contacts were deposited via sputtering. In the patterned Hall bars, the current is applied along the $[1\,\bar{1}\,0]$ or $[\bar{1}\,\bar{1}\,2]$ direction and the field along the out-of-plane [1 1 1] direction.

DATA AVAILABILITY

The data sets generated and/or analyzed during the current study are available from the corresponding author on reasonable request.

Received: 15 November 2020; Accepted: 10 April 2021;
Published online: 12 May 2021

REFERENCES

1. Mehta, V. & Suzuki, Y. Ferromagnetism enhanced by structural relaxation of biaxially compressed $LaCoO_3$ films. *J. Appl. Phys.* **109**, 07D717 (2011).
2. Sanders, T. D. Magnetism in epitaxial $PrCoO_3$ and $Pr_{0.7}Y_{0.3}CoO_3$ thin films. *J. Magn. Magn. Mater.* **451**, 654–659 (2017).
3. Wang, X. R. Imaging and control of ferromagnetism in $LaMnO_3/SrTiO_3$ heterostructures. *Science* **249**, 716–719 (2015).
4. Pedroso, A. L. Strain-induced magnetic transition in $CaMnO_3$ ultrathin films. *Phys. Rev. B* **102**, 085432 (2020).
5. Gozar, A. et al. High-temperature interface superconductivity between metallic and insulating copper oxides. *Nature* **445**, 782–785 (2008).
6. Osada, M. et al. A superconducting praseodymium nickelate with infinite layer structure. *Nano Lett.* **20**, 5735–5740 (2020).
7. Herklotz, A., Rata, A. D., Schultz, L. & Dorr, K. Reversible strain effect on the magnetization of $LaCoO_3$ films. *Phys. Rev. B* **79**, 092409 (2009).
8. Mehta, V. V. et al. Long-range ferromagnetic order in $LaCoO_{3-\delta}$ epitaxial films due to the interplay of epitaxial strain and oxygen vacancy ordering. *Phys. Rev. B* **91**, 144418 (2014).
9. Liu, H. et al. Nature of ferromagnetic ordered state in $LaCoO_3$ epitaxial nano-thin film on $LaAlO_3$ substrate. *J. Alloy Compd.* **594**, 158–164 (2014).
10. Mehta, V. V. et al. Ferrimagnetism in $PrCoO_3$ epitaxial films. *Phys. Rev. B* **87**, 020405 (2013).
11. Doennig, D., Pickett, W. E. & Pentcheva, R. Confinement-driven transitions between topological and Mott phases in$(LaNiO_3)_N/(LaAlO_3)_M$ (111) superlattices. *Phys. Rev. B* **89**, 121110 (2014).
12. Rüegg, A., Mitra, C., Demkov, A. A. & Fiete, G. A. Electronic structure of $(LaNiO_3)_2/(LaAlO_3)_N$ heterostructures grown along [111]. *Phys. Rev. B* **85**, 245131 (2012).
13. Rüegg, A., Mitra, C., Demkov, A. A. & Fiete, G. A. Lattice distortion effects on topological phases in $(LaNiO_3)_2/(LaAlO_3)_N$ heterostructures grown along the [111] direction. *Phys. Rev. B* **88**, 115146 (2013).
14. Yang, K.-Y. et al. Possible interaction-driven topological phases in (111) bilayers of $LaNiO_3$. *Phys. Rev. B* **84**, 201104 (2011).
15. Son, J. et al. Low-dimensional Mott material: transport in ultrathin epitaxial $LaNiO_3$ films. *Appl. Phys. Lett.* **96**, 062114 (2010).
16. Yoo, H. K. et al. Latent instabilities in metallic $LaNiO_3$ films by strain control of Fermi-surface topology. *Sci. Rep.* **5**, 8746 (2015).
17. Moon, E. J. et al. Strain-dependent transport properties of the ultra-thin correlated metal, $LaNiO_3$. *N. J. Phys.* **13**, 073037 (2011).
18. Fowlie, J. et al. Conductivity and local structure of $LaNiO_3$ thin films. *Adv. Mater.* **29**, 18 (2017).
19. Fowlie, J. et al. Thickness-dependent perovskite octahedral distortions at heterointerfaces. *Nano Lett.* **19**, 4188–4194 (2019).
20. Scherwitzl, R. et al. Metal-insulator transition in ultrathin $LaNiO_3$ films. *Phys. Rev. Lett.* **106**, 246403 (2011).
21. Gray, A. X. et al. Insulating state of ultrathin epitaxial $LaNiO_3$ thin films detected by hard x-ray photoemission. *Phys. Rev. B* **87**, 075104 (2011).
22. Sakai, E. et al. Gradual localization of Ni 3d-states in $LaNiO_3$ ultrathin films induced by dimensional crossover. *Phys. Rev. B* **87**, 075132 (2013).
23. Asaba, T. et al. Unconventional ferromagnetism in epitaxial (111) $LaNiO_3$. *Phys. Rev. B* **98**, 121105 (2018).
24. Vailionis, A. et al. Symmetry and lattice mismatch induced strain accommodation near and away from correlated perovskite interfaces. *Appl. Phys. Lett.* **105**, 131906 (2014).
25. Stepanov, S. A. Advances in computational methods for x-ray and neutron optics. *Proc. SPIE* **5536**, 16–26 (2004).

26. Torrance, J., Lacorre, P., Nazzal, A., Ansaldo, E. & Niedermeyer, C. Systematic study of insulator-metal transitions in perovskites $RNiO_3$ (R=Pr,Nd,Sm,Eu) due to closing of charge-transfer gap. *Phys. Rev. B* **45**, 8209–8212 (1993).
27. Hauser, A. J. et al. Correlation between stoichiometry, strain, and metal-insulator transitions of $NdNiO_3$ films. *Appl. Phys. Lett.* **106**, 092104 (2015).
28. Everhardt, A. S., Matzen, S., Domingo, N., Catalan, G. & Noheda, B. Ferroelectric domain structures in low-strain $BaTiO_3$. *Adv. Electron. Mater.* **2**, 1500214 (2016).
29. Zubko, P., Gariglio, S., Gabay, M., Ghosez, P. & Triscone, J.-M. et al. Interface physics in complex oxide heterostructures. *Annu. Rev. Condens. Matter Phys.* **2**, 141–165 (2011).
30. Yang, M.-M. et al. Piezoelectric and pyroelectric effects induced by interface polar symmetry. *Nature* **584**, 377–381 (2020).
31. Kim, T. H. et al. Polar metals by geometric design. *Nature* **533**, 68 (2016).
32. Kim, J. R. et al. Stabilizing hidden room-temperature ferroelectricity via metastable atomic distortion pattern. *Nat. Commun.* **11**, 4944 (2020).
33. Anada, M. et al. Spatial coherence of the insulating phase in quasi-two-dimensional $LaNiO_3$ films. *Phys. Rev. B* **98**, 014105 (2018).
34. Sanchez, R. D. et al. Metal-insulator transition in oxygen-deficient $LaNiO_{3-x}$ perovskites. *Phys. Rev. B* **54**, 16574 (1996).
35. Brenig, W., Döhler, G. H. & Heyszenau, H. Hopping conductivity in highly anisotropic systems. *Philos. Mag.* **27**, 1093–1103 (1973).
36. Nagaosa, N., Sinova, J., Onoda, S., MacDonald, A. H. & Ong, N. P. Anomalous Hall effect. *Rev. Mod. Phys.* **82**, 1539–1592 (2010).
37. Winder, G., Segal, A., Karpovski, M., Shelukhin, V. & Gerber, A. Probing Co/Pd interfacial alloying by the extraordinary Hall effect. *J. Appl. Phys.* **118**, 173901 (2015).
38. Keskin, V. et al. Temperature and Co thickness dependent sign change of the anomalous Hall effect in Co/Pd multilayers: an experimental and theoretical study. *Appl. Phys. Lett.* **102**, 022416 (2013).
39. Izumi, M., Nakazawa, K., Bando, Y., Yoneda, Y. & Terauchi, H. Magnetotransport of $SrRuO_3$ thin film on $SrTiO_3$(001). *J. Phys. Soc. Jpn.* **66**, 3893–3900 (1997).
40. Groenendijk, D. J. et al. Berry phase engineering at oxide interfaces. *Phys. Rev. Res.* **2**, 0233404 (2020).
41. Wang, L. et al. Controllable thickness inhomogeneity and berry curvature engineering of anomalous Hall effect in $SrRuO_3$ ultrathin films. *Nano Lett.* **20**, 2468–2477 (2020).
42. Catalan, G., Seidel, J., Ramesh, R. & Scott, J. F. Domain wall nanoelectronics. *Rev. Mod. Phys.* **84**, 119–156 (2012).
43. Guronnet, J., Gaponenko, I., Gariglio, S. & Paruch, P. Conduction at domain walls in insulating $Pb(Zr_{0.2}Ti_{0.8})O_3$ thin films. *Adv. Mater.* **23**, 5377–5382 (2011).
44. Seidel, J. et al. Conduction at domain walls in oxide multiferroics. *Nat. Mater.* **8**, 229–234 (2009).
45. Kim, W. J. et al. Unconventional anomalous Hall effect from antiferromagnetic domain walls of $Nd_2Ir_2O_7$ thin film. *Phys. Rev. B* **98**, 125103 (2018).
46. Nakajima, Y., Syers, P., Wang, X., Wang, R. & Paglione, J. One-dimensional edge state transport in a topological Kondo insulator. *Nat. Phys.* **12**, 213–217 (2016).
47. Checkelsky, J. G., Ye, J., Onose, Y., Iwasa, Y. & Tokura, Y. Dirac-fermion-mediated ferromagnetism in a topological insulator. *Nat. Phys.* **8**, 729–733 (2012).
48. Goodenough, J. B. *Magnetism and the Chemical Bond* (Wiley Interscience, 1963).

ACKNOWLEDGEMENTS

The research was supported by the US Department of Energy, Director, Office of Science, Office of Basic Energy Sciences, Division of Materials Sciences and Engineering under Contract No. DESC0008505. Part of this work was performed at the Stanford Nano Shared Facilities (SNSF), supported by the National Science Foundation under award no. EECS-1542152. This material is based on work supported by the National Science Foundation Graduate Research Fellowship grant number DGE-1656518. LJR was supported by the Air Force Office of Scientific Research under Grant No. FA9550-20-1-0293. This research used resources of the Advanced Light Source, which is a DOE Office of Science User Facility under contract no. DE-AC02-05CH11231. Use of the Stanford Synchrotron Radiation Lightsource, SLAC National Accelerator Laboratory, is supported by the US Department of Energy, Office of Science, Office of Basic Energy Sciences under Contract No. DE-AC02-76SF00515

AUTHOR CONTRIBUTIONS

M.M.K. grew all samples, acquired, analyzed, and interpreted XRD, XAS, and transport data; A.V. performed x-ray diffraction simulations; L.J.R. acquired and analyzed XRD data; A.M. helped to acquire XRD data; A.T.N. and E.A. helped to acquire XAS data; C.K. and P.S. helped to acquire and analyze XMCD data; M.M.K. and Y.S. designed the experiments and wrote the manuscript. All authors reviewed the final manuscript.

COMPETING INTERESTS

The authors declare no competing interests.

ADDITIONAL INFORMATION

Supplementary information The online version contains supplementary material available at https://doi.org/10.1038/s41535-021-00345-2.

Correspondence and requests for materials should be addressed to M.M.K. or Y.S.

Reprints and permission information is available at http://www.nature.com/reprints

Publisher's note Springer Nature remains neutral with regard to jurisdictional claims in published maps and institutional affiliations.